moderate labeling ability. Scale bar is drawn at the bottom. DMSB, dimethylamino-styryl-benzothiazole.

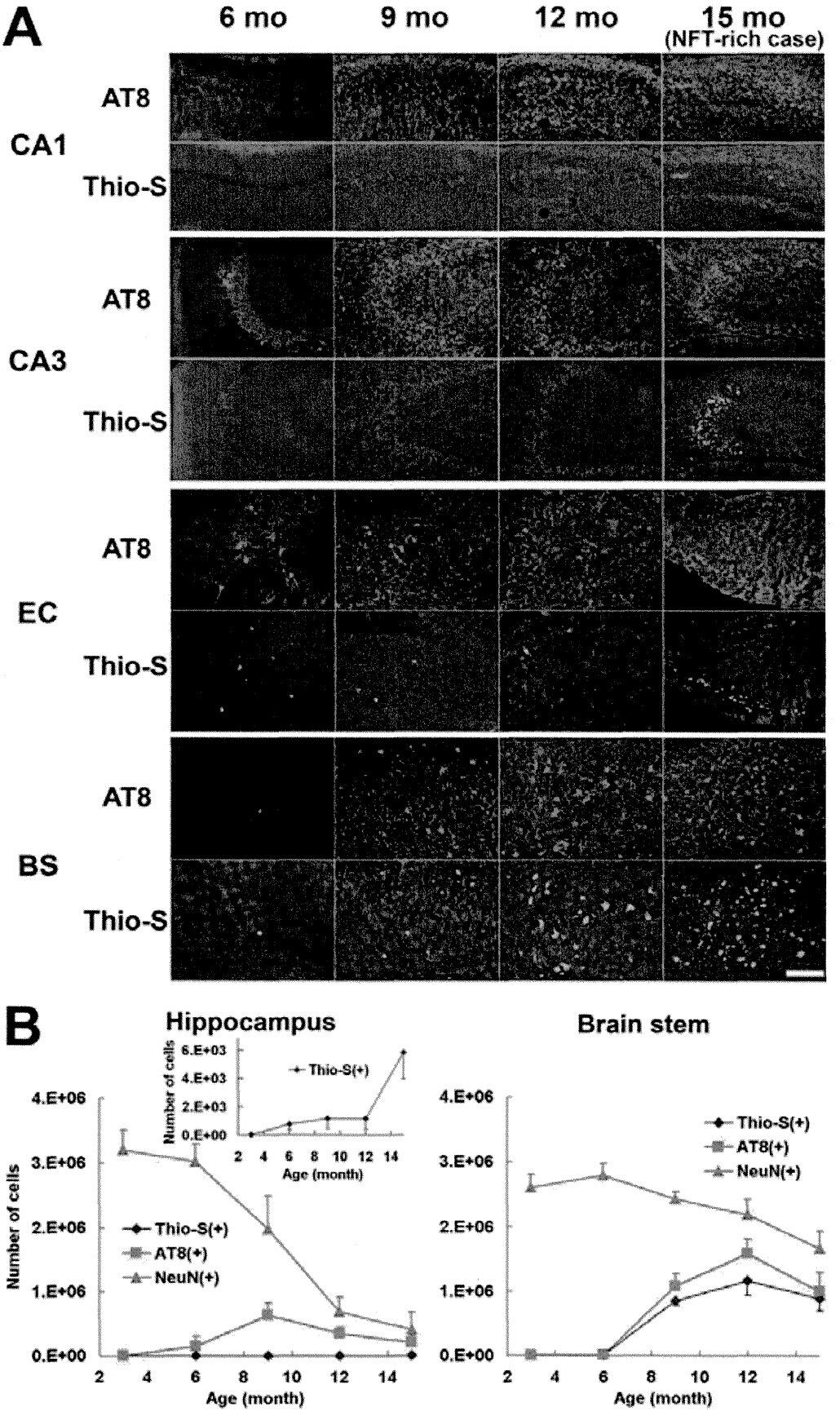
A
6 mo
9 mo
12 mo
15 mo
(NFT-rich case)
AT8
CA1
Thio-S
AT8
CA3
Thio-S
AT8
EC
Thio-S
AT8
BS
Thio-S
B
Hippocampus
Brain stem
Number of cells
Thio-S(+)
AT8(+)
NeuN(+)
Age (month)
4.E+06
3.E+06
2.E+06
1.E+06
0.E+00
6.E+03
4.E+03
2.E+03
0.E+00
2 4 6 8 10 12 14

Figure S2 | Distribution of FSB-positive NFT-like lesions in PS19 mice, related to Figure 3. (A) Accumulation of phosphorylated tau and thioflavin-S (Thio-S) positive tau fibrils in the hippocampus, entorhinal cortex (EC) and brain stem (BS) of PS19 mice at 6-15 months of age. Samples from a 15-month-old mouse shown here exhibited the most abundant hippocampal/entorhinal inclusions detected by thioflavin-S. Numerous intraneuronal tau fibrils doubly positive for AT8 and thioflavin-S accumulate with advancing age primarily in the brain stem and spinal cord of these mice, but a large subset of AT8-immunoreactive tau deposits are thioflavin-S negative in the hippocampus, resembling "pretangles" in human brains. **(B)** Total numbers of NeuN-, AT8- and thioflavin-S-positive neurons in the entire hippocampus and brain stem of PS19 mice at 3-15 months of age. The numbers were calculated based on the density of positive neurons in slices and individual volume of these structures measured by *in vivo* MRI. The number of AT8-positive neurons was estimated by counting somatic labelings. These data indicate that hippocampal neurons in PS19 mice are likely to be vulnerable to either neurotoxicity of relatively immature tau assemblies or abolishment of physiological functions of tau by its phosphorylation and consequent dissociation from microtubules. Scale bar: 200 μm (**A**).

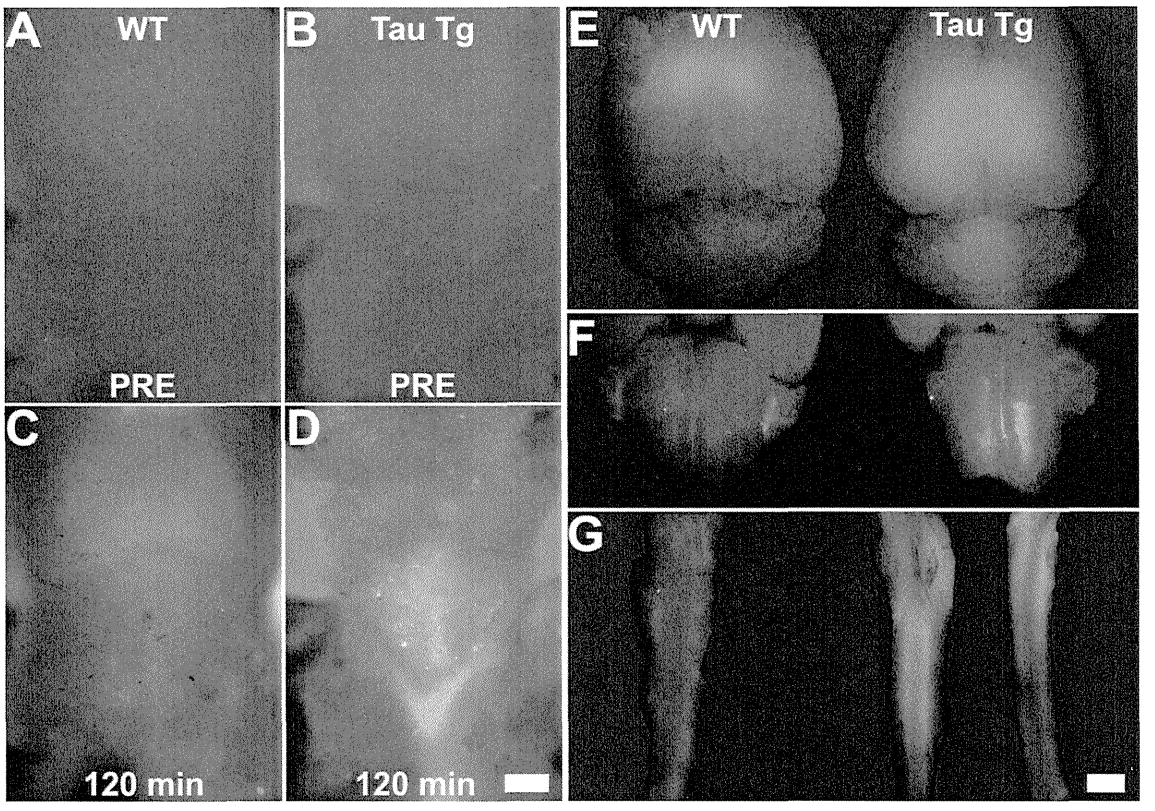

Figure S3. *In vivo* and *ex vivo* distributions of intravenously administered PBB5 (1 mg/kg) in mice, related to Figure 4. **(A-D)** Near-infrared fluorescence images of shaven heads of living non-Tg WT (**A**, **C**) and PS19 (Tg; **B**, **D**) mice at 12 months of age. Relative to the baseline autofluorescence before the tracer injection (PRE; **A**, **B**), signals were increased particularly in the posterior portion of PS19 mouse head (compare **C** and **D**). The fluorescence in the Tg mouse was remarkably augmented in an area above the slit between the skull and first vertebra (**D**). **(E-G)** *Ex vivo* observation of WT (left) and PS19 (Tg; right) mouse brains (**E**, **F**) and spinal cords (**G**) removed after 120-min *in vivo* imaging. Although there were no convincing differences in fluorescence signal intensities between top-view images of the WT and Tg mice (**E**), bottom views of brain stems indicated a notably increased accumulation of PBB5 in the Tg mouse in comparison with the WT control (**F**). Enhanced labeling with the injected tracer was also captured in the spinal cord of the Tg mouse (**G**). Scale bars: 2.5 mm

(**A**-**D**); 2 mm (**E**-**G**).

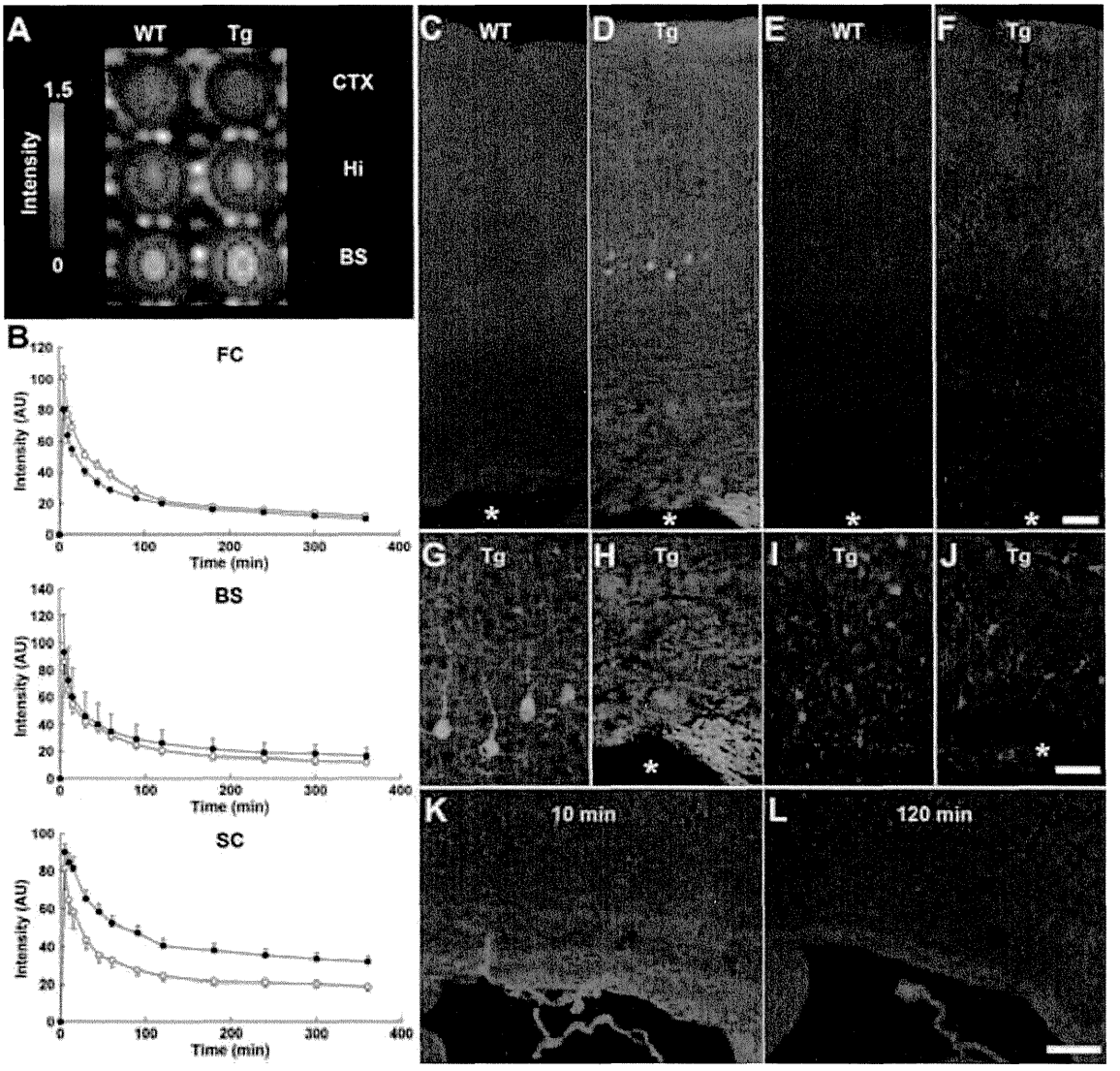

Figure S4. *Ex vivo* and *in vivo* assays of fluorescence signals from intravenously injected PBB5 in mouse brains by pulsed laser optics, related to Figure 4. (A) Fluorescence intensity was measured in neocortical (CTX), hippocampal (Hi) and brain stem (BS) tissues obtained from 12-month-old non-Tg WT and PS19 (Tg) mice at 20 hr after the administration of PBB5 (0.1 mg/kg). The intensity was normalized by the BS value in the Tg mouse. **(B)** Time-intensity curves in near-infrared pulsed laser fluorescence imaging of living mice after intravenous administration of PBB5 (0.1 mg/kg). Dynamic data in the frontal cortex (FC), BS and spinal cord (SC) ROIs of non-Tg WT (open circles) and PS19 Tg (closed circles) mice are displayed. The

fluorescence intensity in an arbitrary unit (AU) was determined based on the laser power and integration time in each scan. Vertical bars represent SEs. **(C-J)** Immunostaining with anti-phospho-tau antibody AT8 (**C, D, G, H**) and anti-Iba1 antibody (**E, F, I, J**) for frontal cortical sections obtained from 10-month-old WT (**C, E**) and PS19 Tg (**D, F, G-J**) mice. Asterisks denote lateral ventricle. Accumulation of phosphorylated tau in neurons and activation of microglia are noticeable from superficial cortical layers to paraventricular area. High-power photomicrographs in the middle layers (**G, I**) and vicinity of lateral ventricle (**H, J**) are also displayed. (**K, L**) *Ex vivo* near-infrared fluorescence signals in the WT mouse frontal cortex at 10 (**K**) and 120 (**L**) min after intravenous injection of PBB5. Intense signals were observed in choroid plexus and close proximity of lateral ventricle at 10 min, suggesting that PBB5 might undergo transfer to the frontal cortex via lateral ventricles, similar to other charged small molecules exemplified by Mn^{2+} (Silva et al., 2004). Decrease in initial uptake of PBB5 into the Tg frontal cortex could accordingly stem from impaired delivery of PBB5 to the brain tissue through ependyma and attenuated transport through neuronal plasma membrane in this brain area. Fluorescence was diminished and became more homogenous in the field of view at 120 min. Scale bars: 100 μm (**C-F**); 50 μm (**G-J**); 100 μm (**K, L**).

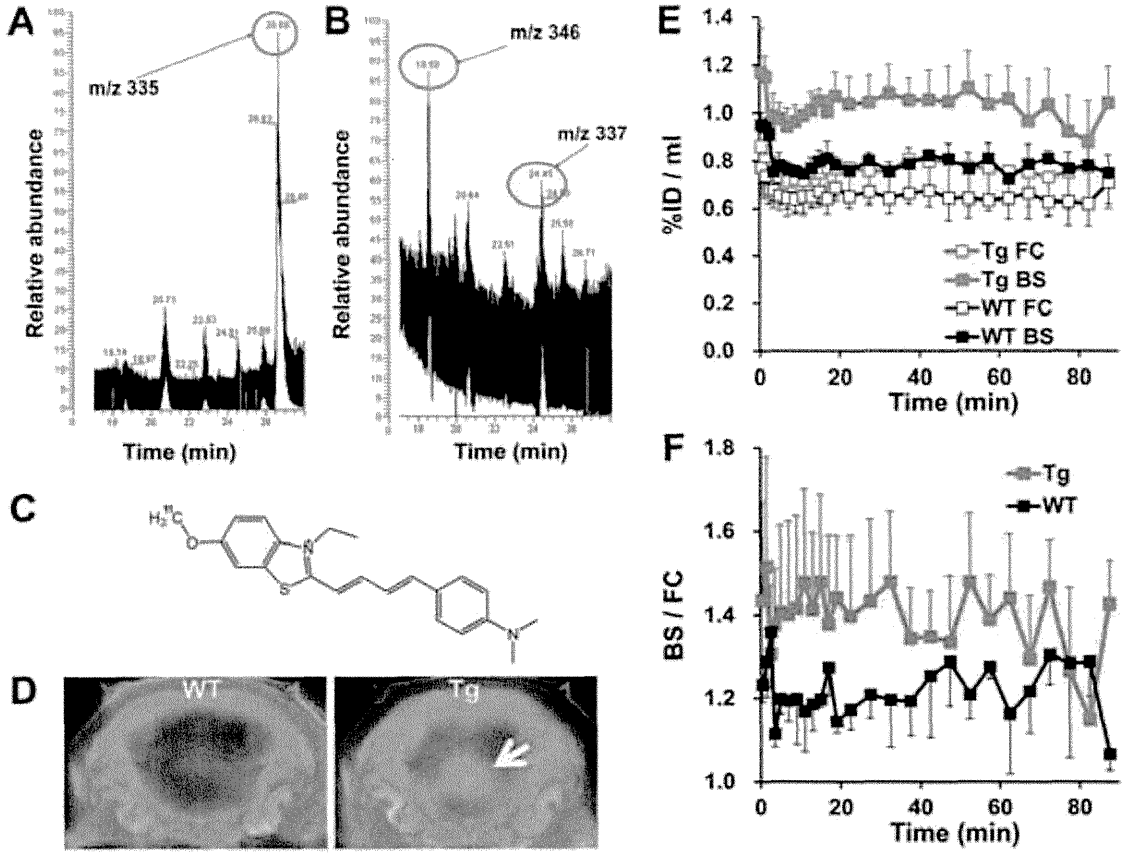

Figure S5. Metabolic profile of PBB5 and *in vivo* PET imaging of mouse brains with [^{11}C]mPBB5, related to Figure 6. (A) Standard analysis of PBB5 dissolved in DMSO. The mass-to-charge ratio (m/z) is indicated for an originally charged, unmetabolized compound (molecular weight = 335 Da). **(B)** Major elements contained in the largest metabolite fraction in plasma samples from non-Tg WT mice at 5 min after intravenous tracer injection. The peak at m/z 337 is likely to correspond to an electrically neutral metabolite with a molecular weight of 336 Da. **(C)** Chemical structure of [^{11}C]mPBB5. **(D)** Coronal PET images showing distribution of [^{11}C]mPBB5 in WT (left) and PS19 Tg (right) mouse brains containing the cerebellum and pons (sectioned at 6 mm posterior to the bregma). Images were generated by averaging dynamic data at 30 – 90 min after intravenous injection of the radiotracer, and were superimposed on the MRI template. An increased retention of [^{11}C]mPBB5 was

observed in the brain stem of PS19 mice (arrow) relative to WT controls following intravenous administration. **(E, F)** Time-radioactivity curves (**E**) for [^{11}C]mPBB5 in the frontal cortex (FC) and brain stem (BS) and BS-to-FC ratio of radioactivity (**F**) over the imaging time in PS19 Tg (red symbols) and WT (black symbols) mice (n = 3 each). The entry of [^{11}C]mPBB5 into the brain displayed a biphasic pattern followed by a very slow washout, presumably reflecting its complex pharmacokinetics as anticipated by the metabolic profile of nonradioactive PBB5. Based on the brain stem radioactivity normalized by the frontal cortex value after the injection of [^{11}C]mPBB5, the levels of this ligand showed a tendency to increase in PS19 mice compared to WT mice ($p < 0.1$ for the interaction between time and genotype by 2-way repeated-measures ANOVA). Vertical bars in the graphs denote SEs.

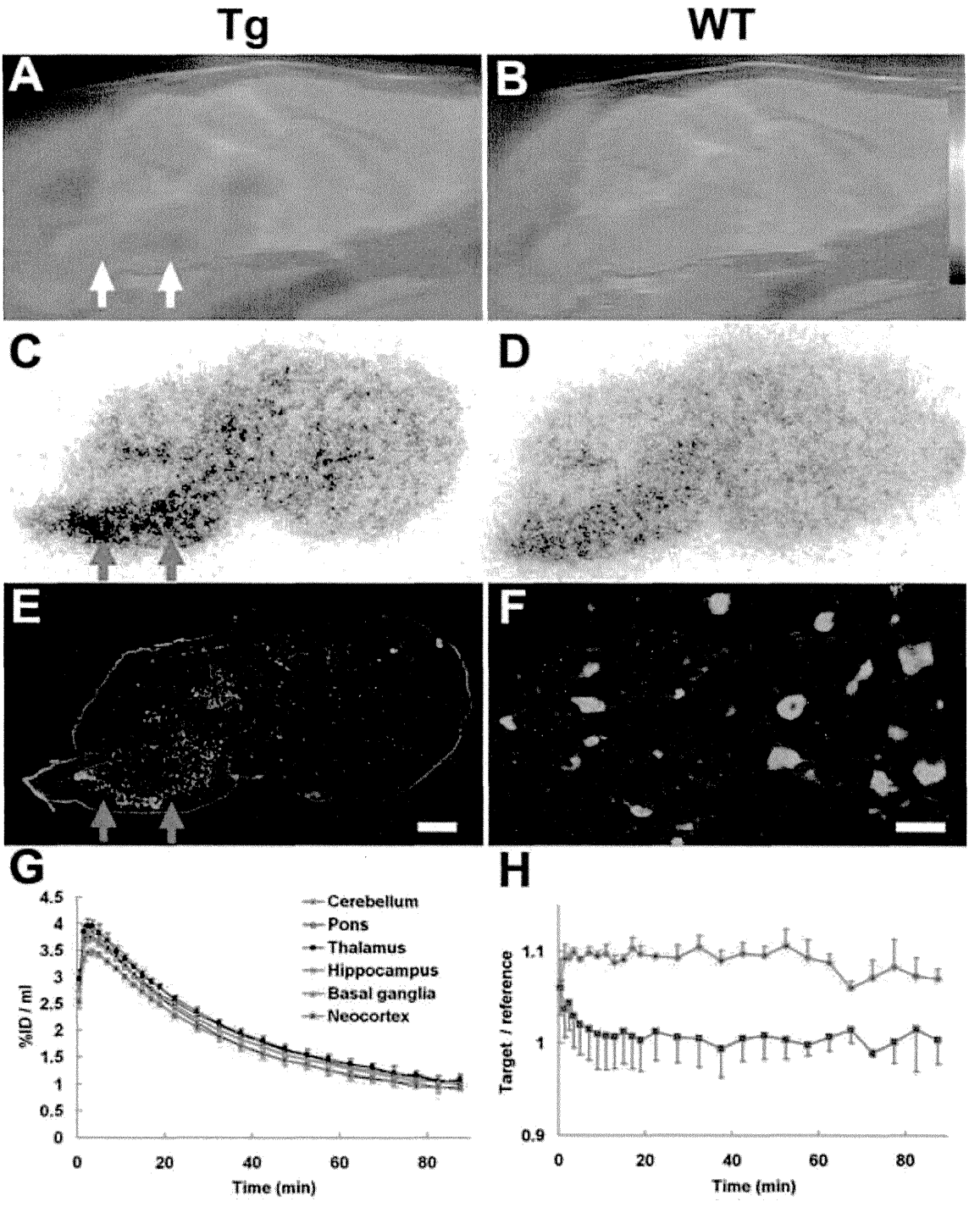

Figure S6. ***In vivo*** **PET and** ***ex vivo*** **autoradiographic imaging in PS19 (Tg; left) and nonTg WT (right) mice using [^{11}C]PBB2, related to Figure 6. (A, B)** Sagittal PET images generated by averaging dynamic scan data at 60-90 min after tracer administration. The images were overlaid on the MRI template. The data were scaled in

a range of 0 to 1.5% of injected dose (ID) per ml tissue. Arrows indicate increased tracer binding in the brain stem. **(C, D)** *Ex vivo* autoradiographic images in the mice shown in **A** and **B**. Arrows indicate intensification of radiolabeling in PS19 mice. **(E, F)** FSB staining of the autoradiographic sample shown in **C** at low (**E**) and high (**F**) magnifications. Accumulation of NFT-like inclusions in the brain stem (arrows in **E**) is displayed in a high-power view (**F**). **(G)** Time-radioactivity curves in multiple brain areas of WT mice (n = 5). **(H)** Brain stem-to-striatum ratio of radioactivity over the imaging time in PS19 (red symbols) and WT (blue symbols) mice (n = 5 each). Vertical bars in the graphs denote SEs. Scale bars: 1 cm (**A-E**); 50 μm (**F**).

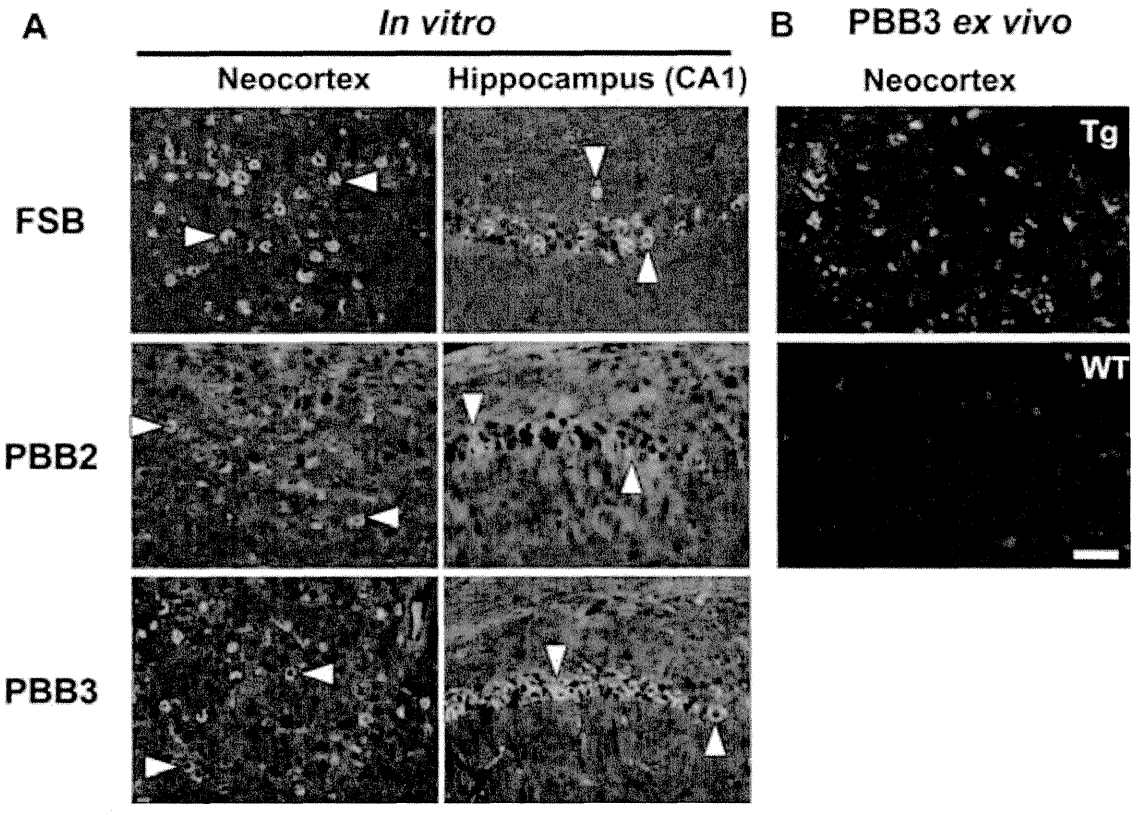

Figure S7. *In vitro* and *ex vivo* binding of PBBs to neocortical and hippocampal tau inclusions in rTg4510 mice, related to Figure 6. (A) *In vitro* fluorescence staining of neocortical and hippocampal sections generated from 8-month-old rTg4510 mice. FSB, PBB2 and PBB3 labeled numerous neuronal aggregates, but no staining was observed in age-matched WT mouse samples (data not shown). **(B)** *Ex vivo* fluorescence labeling of the neocortex of 10-month-old rTg4510 (upper panel) and 15-month-old WT (lower panel) mice with PBB3. Mice received intravenous injection of 1 mg/kg PBB3, and brain tissue was collected at 30 min after compound injection. Scale bar: 50 μm (**A, B**).

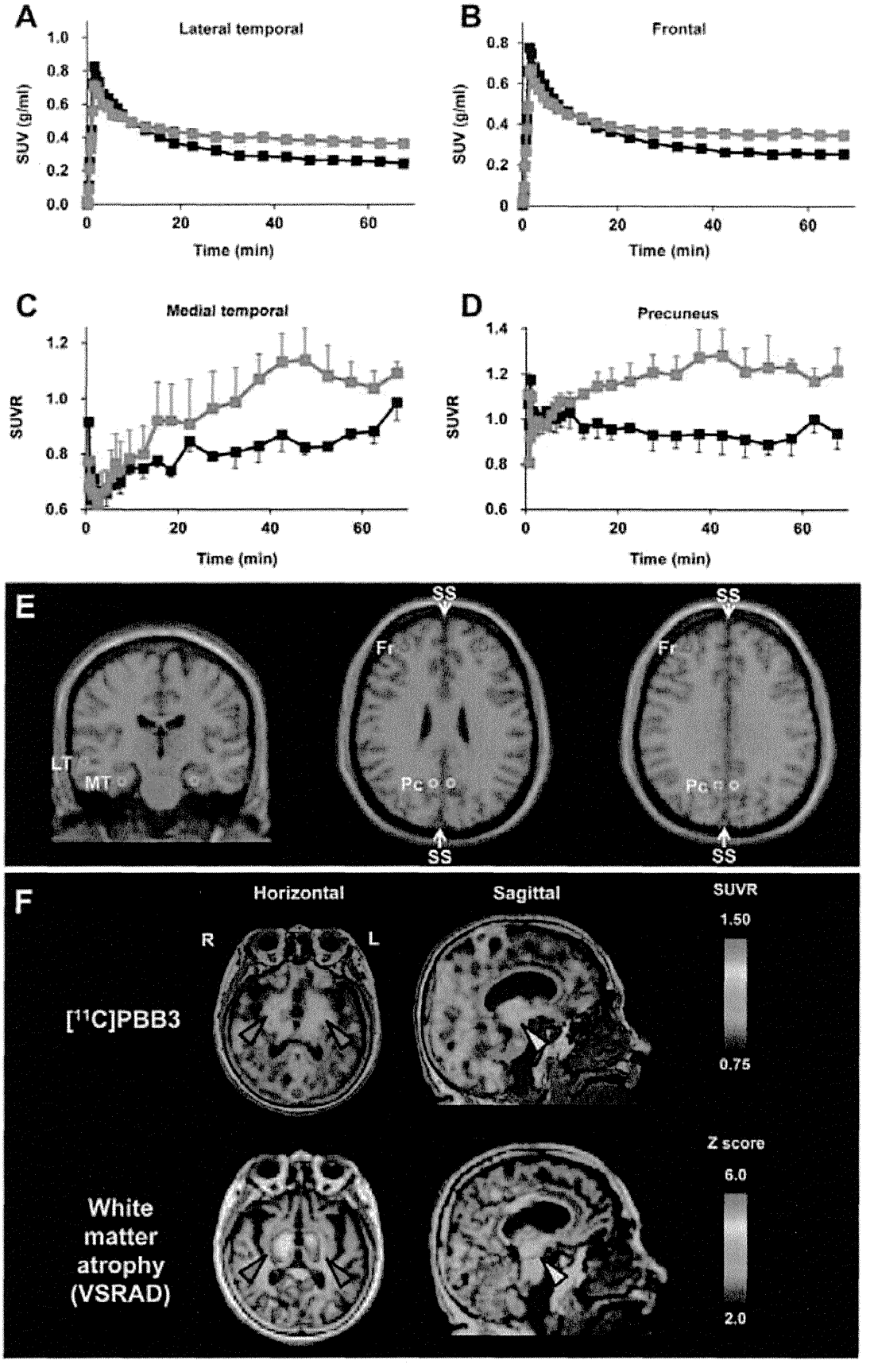
A
Lateral temporal
SUV (g/ml)
Time (min)
B
Frontal
SUV (g/ml)
Time (min)
C
Medial temporal
SUVR
Time (min)
D
Precuneus
SUVR
Time (min)
E
SS
Fr
LT
MT
Pc
SS
F
Horizontal
Sagittal
SUVR
1.50
0.75
R
L
[11C]PBB3
Z score
6.0
2.0
White matter atrophy (VSRAD)

Figure S8. PET and MRI data in humans, related to Figure 9. (A, B) Comparisons of time-radioactivity curves in the lateral temporal (**A**) and frontal (**B**) regions of normal controls (black symbols and lines; n = 3) and AD patients (red symbols and lines; n = 3). Following initial uptake into the brain, [^{11}C]PBB3 retention continuously declined over time in normal controls. This is consistent with the finding that HPLC assays of plasma samples indicated that major metabolites of [^{11}C]PBB3 were relatively hydrophilic having shorter retention times than unmetabolized compound (data not shown) and were accordingly presumed not to undergo efficient transfer through BBB. **(C, D)** Target-to-cerebellum ratio of SUV (SUVR) in the medial temporal region (**C**) and precuneus (**D**) of normal controls (black symbols and lines; n = 3) and AD patients (red symbols and lines; n = 3). Vertical bars in graphs denote SE. **(E)** Representative coronal (left) and horizontal (middle and right) MRI images showing standard anatomical space and locations of VOIs in the medial temporal (MT), lateral temporal (LT), precuneus (Pc) and frontal (Fr) areas. Superior sagittal dural sinus (SS) is indicated by arrows. **(G)** Relationship between tau accumulation and subcortical atrophy in a patient with clinical diagnosis of corticobasal syndrome. Horizontal and sagittal [^{11}C]PBB3-PET images are identical to those in Figure 9, and are compared to Z score maps generated by VSRAD for voxels segmented as white matter. Right-side dominant PET signals and volume reduction were observed in the basal ganglia (red arrowheads), and radioligand retention in the midbrain (yellow arrowhead) was accompanied by local atrophy.

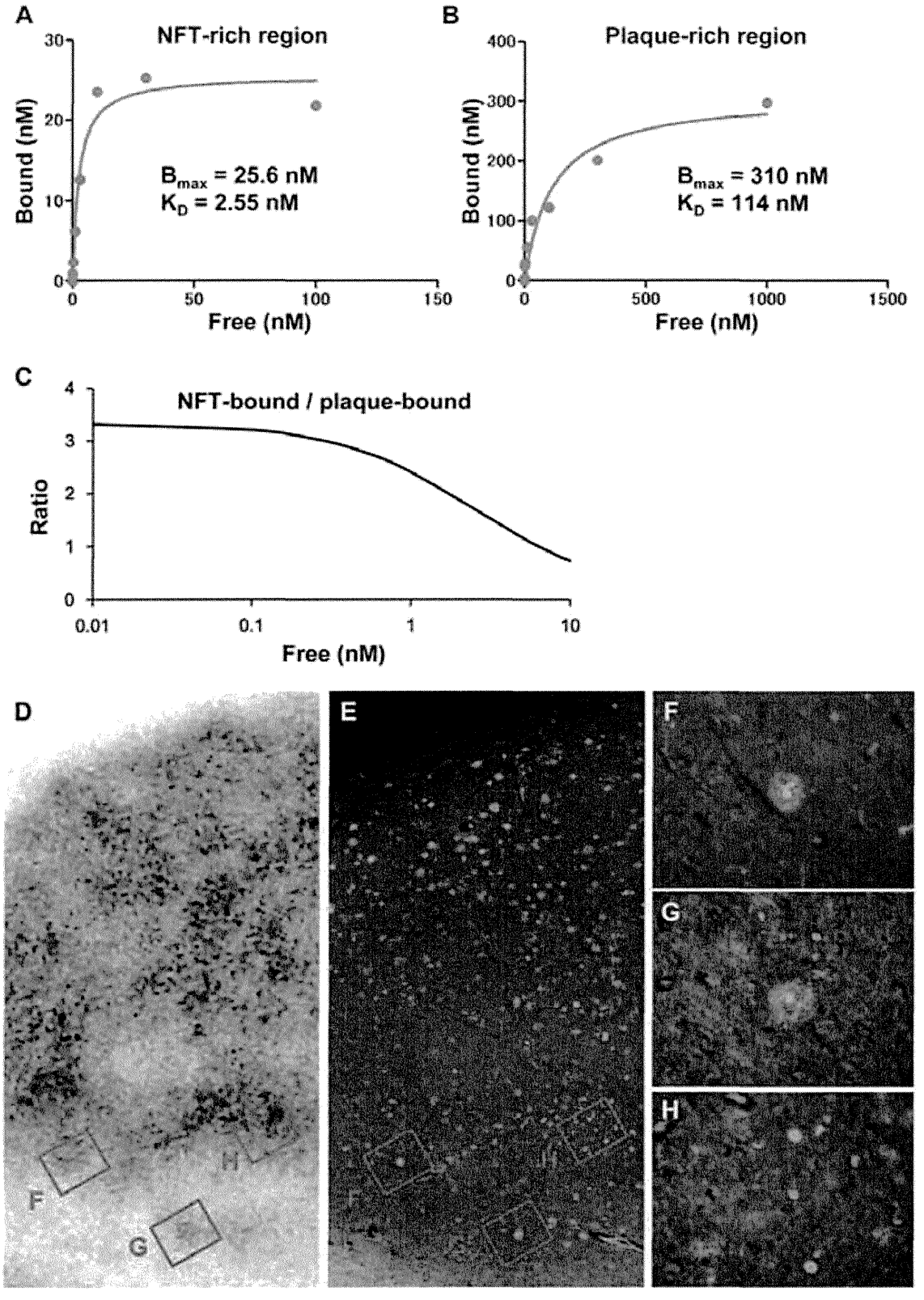

Figure S9. Autoradiographic binding of [^{11}C]PBB3 to plaque- and tangle-rich

regions in AD brains, related to Figures 7, 8 and 9. (A, B) Saturation binding plots showing reaction of PBB3 at different concentrations with the hippocampal CA1 (**A**) and gray matter of the lateral temporal cortex (**B**) enriched with NFTs and senile plaques, respectively. B_{max} and K_D values estimated by a homologous displacement model are displayed in graphs. Red lines represent regressions. (**C**) Simulation plot of ratio of NFT-bound PBB3 to plaque-bound PBB3 against concentration of free PBB3. The ratio was determined on the assumption that target tissue contained high-affinity, low-capacity binding sites (B_{max} = 25 nM, K_D = 2.5 nM) and low-affinity, high-capacity binding sites (B_{max} = 300 nM, K_D = 100 nM) primarily composed of tau and Aβ fibrils, respectively. (**D-H**) [^{11}C]PBB autoradiography (**D**) and FSB staining (**E-H**) for the same AD neocortical section. FSB staining in areas containing dense cored plaques (**F, G**) and numerous NFTs (**H**) are indicated by red squares in Panels **D** and **E**, and are displayed as high-power photomicrographs in Panels **F-H**. Areas containing dense core plaques but lacking abundant NFTs were only modestly radiolabeled with [^{11}C]PBB3 (**D-G**). By contrast, relatively deep gray matter layers enriched with NFTs and neuropil threads but no cored plaques were intensely radiolabeled (**D, E, H**).

Table S1. Fluorescence and binding properties of β-sheet ligands for assemblies from synthetic Aβ peptide and recombinant tau protein, related to Figure 1.

Compound	λ_{ex} & λ_{em} (nm)		EC_{50} (nM)		EC_{50}(Aβ) / EC_{50}(tau)
	Aβ40	T40	Aβ40	T40	
Thioflavin-T	445 & 495	445 & 485	1,463 ± 459	818 ± 231	1.8
PBB5	635 & 685	630 & 685	1,217 ± 850	126 ± 67	9.7
PBB1	440 & 565	515 & 565	4,109 ± 764	402 ± 352	10.2

λ_{ex} and λ_{em} are optimal excitation and detection wavelengths, respectively, in the fluorometry of compounds bound to assembled Aβ40 and T40 (longest tau isoform consisting of 441 amino acid residues). EC_{50} (mean ± SE) denotes an effective concentration of the compound yielding half-maximal fluorescence intensity in the saturation plot (Okamura et al., 2005). The ratio of EC_{50} for Aβ40 fibrils to that for T40 fibrils is shown in the far-right column.

Supplemental Discussion

Relationship between structures of β-sheet ligands and their reactivity with diverse tau lesions

It is known that most tau-positive frontotemporal lobar degeneration (FTLD) and related non-AD tauopathies are biochemically characterized by insoluble and hyperphosphorylated aggregates of three of six tau isoforms with a predominance of either three or four repeat domains, which are distinct from the assembly of all six tau isoforms in the paired helical filaments found in AD brains (Ballatore et al., 2007). Hence, the present findings imply that three classes of amyloidogenic components, Aβ, AD tau amyloid and non-AD tau amyloid, form cross-β structures with distinct alignment and/or dimensions.

According to X-ray diffraction analyses, the "side chain reflection", which is typically close to 10-11 Å (Fändrich et al., 2002), was shown to be lengthened to 13 Å in the assembly from recombinant tau proteins with four repeat domains and a P301S mutation (Berriman et al., 2003), suggesting an increased intersheet spacing due to a large proportion of bulky side chains contained in the cross-β-forming core of the tau molecule. Despite previous reports supporting binding of thioflavin-T and Congo red to amyloid fibrils such that their long axes are parallel (Krebs et al., 2005), there have been indications of a dual mode of ligand-amyloid interactions (Wu et al., 2007), and we propose here that there is an additional possibility wherein the ligands lie perpendicular to the fibril axis and override the spacing between β-sheets. This notion may provide a plausible reason why PBBs, FSB and thioflavin-S, with the long axes of their core structure sufficiently exceeding 13 Å in length, are capable of binding to a variety of tau

aggregates (Fig. S1). Tau proteins in the brain usually consist of three isoforms with three repeat domains (3RTs) and three isoforms with four repeat domains (4RTs), and AD NFTs are composed of all six isoforms, which are distinct from tau assemblies in other non-AD tauopathies formed predominantly by 3RTs (Pick's disease) or 4RTs (CBD and PSP) (Ballatore et al., 2007; Dickson et al., 2011). Based on the reactivity of various β-sheet ligands, the packing dimension of these two classes of tau fibrils may differ, and tau aggregates in PS19 mice are likely to have homology to non-AD type tau fibrils. The structural considerations of the interactions between small ligands and tau/Aβ fibrils would provide a clue for the development of selective radioprobes and anti-aggregation agents counteracting amyloid polymerization.

Accumulation of [^{11}C]PBB3 around dural venous sinuses in humans

Although nonspecific [^{11}C]PBB3-PET signals in control human subjects were generally low, radioligand retention in dural venous sinuses was noticeable in all scanned individuals. This finding resembles a previous report a case exhibiting accumulation of [^{11}C]PIB in venous sinuses (Raymond et al., 2012). However, [^{11}C]PBB3 signals in venous sinuses were much more frequent and consistent, and none of the subjects in the present work showed increased retention of [^{11}C]PIB in sinuses. Our recent PET study has also indicated that [^{11}C]AZD2184, a plaque radioligand (Forsberg et al., 2013) accumulates in dural venous sinuses (Shimada et al., unpublished data). Both [^{11}C]PBB3 and [^{11}C]AZD2184 are composed of methylaminopyridine and hydroxybenzothiazole, but [^{11}C]AZD2184 does not react with tau aggregates. Accumulation of these radioligands in venous sinuses may therefore be unrelated to tau and Aβ pathologies, while there remains the possibility that some proteinaceous

components in cerebrospinal fluid may be trapped in the vicinity of arachnoid granulations protruding into venous sinuses, and may constitute aggregates providing binding sites for these radioligands. The pathophysiological basis of [^{11}C]PBB3 binding to sinuses will be clarified by further postmortem examinations of meningeal samples. In our pilot clinical PET study, quantitative analyses were performed by placing VOIs distant from venous sinuses (Fig. S8E), and future quantifications of multiple VOIs or parametric maps with a larger sample size will elucidate influences of radioactivity spillover from sinuses on neighboring areas.